Supporting Information

Matyszewski et al. 10.1073/pnas.1712860115

SI Materials and Methods

Reagents. Human AIM2^{FL} (residues 1–343), AIM2^{PYD} (residues 1–94) S94C, and ASC^{PYD} (residues 1–106) S106C were cloned into a pET21b vector (Novagen) with an N-terminal MBP-tag and TEVp-recognition site. All proteins were expressed in *Escherichia coli* strain ER2566 and purified as described (1). Labeling of FRET donor or acceptor dyes was also performed as described previously (1). Typical labeling efficiencies were 0.8:1 label:protein or higher. FAM-labeled or unlabeled dsDNA were either commercially obtained (≤72 bp) or via PCR using the MBP gene as a template.

Monte Carlo Simulation. We generated a butterflied, honeycomb-like view of the AIM2^{PYD} filament based on the cryo-EM structure of the ASC^{PYD} filament (2) (Fig. S3*A*; each horizontal side of the honeycomb is still connected in the simulation and the length is infinite). We used a hexagon to represent individual AIM2^{PYD}, as each molecule contains six protein–protein interaction surfaces that participate in filament assembly (1, 2). We then simulated the probability of contiguously filling the horizontal plane of the honeycomb by a different number of AIM2^{PYD} molecules after 10,000 random trials. We used the following assumptions/conditions in our simulation (Fig. S3*A*, see Dataset S2 for code). (*i*) The energetic contributions of the six filament interfaces in AIM2^{PYD} are the same, and the assembly utilizes each interface randomly (thus represented as hexagons in Fig. S3*A*). (*ii*) Each AIM2^{PYD} was sequentially added because our experimental results suggest that the assembly on dsDNA occurs in a stepwise manner (Fig. 2). (*iii*) We allowed new interfaces created by two or more PYDs to be more favorable for another PYD to occupy (increasing shade of blue in Fig. S3*A*). Finally, (*iv*) we defined that the "in-plane" configuration can be achieved in a zig-zag manner without any vertical gap (e.g., Fig. S3*A* 3 in-plane). Of note, the length of unstructured linker between AIM2^{PYD} and AIM2^{Hin} is 51 aa, likely spanning >150 Å. Although we did not explicitly add the possible constraints posed by the linker, considering that the AIM2^{PYD} is 26 Å by 23 Å (Protein Data Bank ID code 407Q), we reasoned that the linker is long enough to allow AIM2^{PYD} to be added to all possible directions.

Mathematical Modeling. To model the AIM2-ASC signaling cascade, we first divided the assembly pathway into nine distinct, measurable processes based our experiments (Fig. S3*B*; see the accompanying figure legend for details), which also resulted in nine rate equations (***simEq. 1–9***; Fig. S3*B*). Of note, because putative nucleation units and fully assembled filaments are indistinguishable in our experiments, we treated both species as polymers in our model (i.e., both species generate FRET signals). This strategy in turn allowed us to minimize the number of fitting parameters. We then used Python scripts to numerically integrate *simEq.* ***1–9*** to model the signaling pathway. To account for various experimental observations such as the threshold behavior in protein concentration dependence and nonlinear dsDNA-length dependence we added the following modifiers when appropriate: *AIM2dsDNA*, *ringBind1*, *ringBind2*, *ASCdnaAIM2*, and *AIM2^{n}DNA* (see where applied for details; Fig. S3*B* legends). The individual rate constants describing these processes (k_1 through k_{11}) were then determined by sequentially fitting each assembly event with least-squares regression. For example, to model AIM2 assembly we first globally fit the results described in Figs. 1*C* and 4*B* (Fig. S3*B*, *a*). We then used the same k_1, k_2, and k_3 to determine *ringBind1* (Fig. 4*E* and Fig. S3*B*, *c*). We assumed that the number of polymers for both AIM2 and ASC are proportional to protein concentrations beyond their thresholds and used binding-site normalized dsDNA concentrations. We also assumed that the ability of dsDNA-bound AIM2^{FL} to accelerate the polymerization of its target is preserved at different AIM2^{PYD} and ASC^{PYD} concentrations (e.g., Fig. S4*B*). The determined fitting parameters are listed in Dataset S1.

To implement the threshold behaviors in protein concentration-dependent assembly (Fig. 1), when normalizing our FRET experimental data to molar concentrations, we subtracted the highest concentration that did not result in filament formation from AIM2^{PYD} and ASC^{PYD} (i.e., "threshold/critical concentration"; 0.25 and 0.5 μM for AIM2^{PYD} and ASC^{PYD}, respectively, as observed in Fig. 1). Additionally, for the "seeding" experiments in which AIM2^{PYD}/ASC^{PYD} polymers accelerate the polymerization of respective monomers (e.g., Figs. 4–6), we subtracted the critical concentration from each "seed," amount and added the equivalent amount to the total monomer concentration. For example, when 5 μM of preassembled AIM2^{PYD} accelerates the polymerization of 2.5 μM AIM2^{PYD} monomers we considered that the concentration of preformed polymers to be 4.75 μM and that of monomers as 2.75 μM. With this method, the final concentration of newly formed polymers is still 2.5 μM, as 0.25 μM is subtracted again due to the threshold behavior.

Additionally, in our final model we applied the rate constants determined for AIM2^{PYD} to describe dsDNA-free AIM2^{FL} and considered ASC^{PYD} as ASC. Thus, the in vitro assembly $t_{\frac{1}{2}}$s determined here are likely slower than those of full-length proteins in vivo. Nonetheless, considering that PYD–PYD interactions are crucial for filament assembly and signaling, we expect our results to scale with in vivo events.

1. Morrone SR, et al. (2015) Assembly-driven activation of the AIM2 foreign-dsDNA sensor provides a polymerization template for downstream ASC. *Nat Commun* 6:7827.

2. Lu A, et al. (2014) Unified polymerization mechanism for the assembly of ASC-dependent inflammasomes. *Cell* 156:1193–1206.

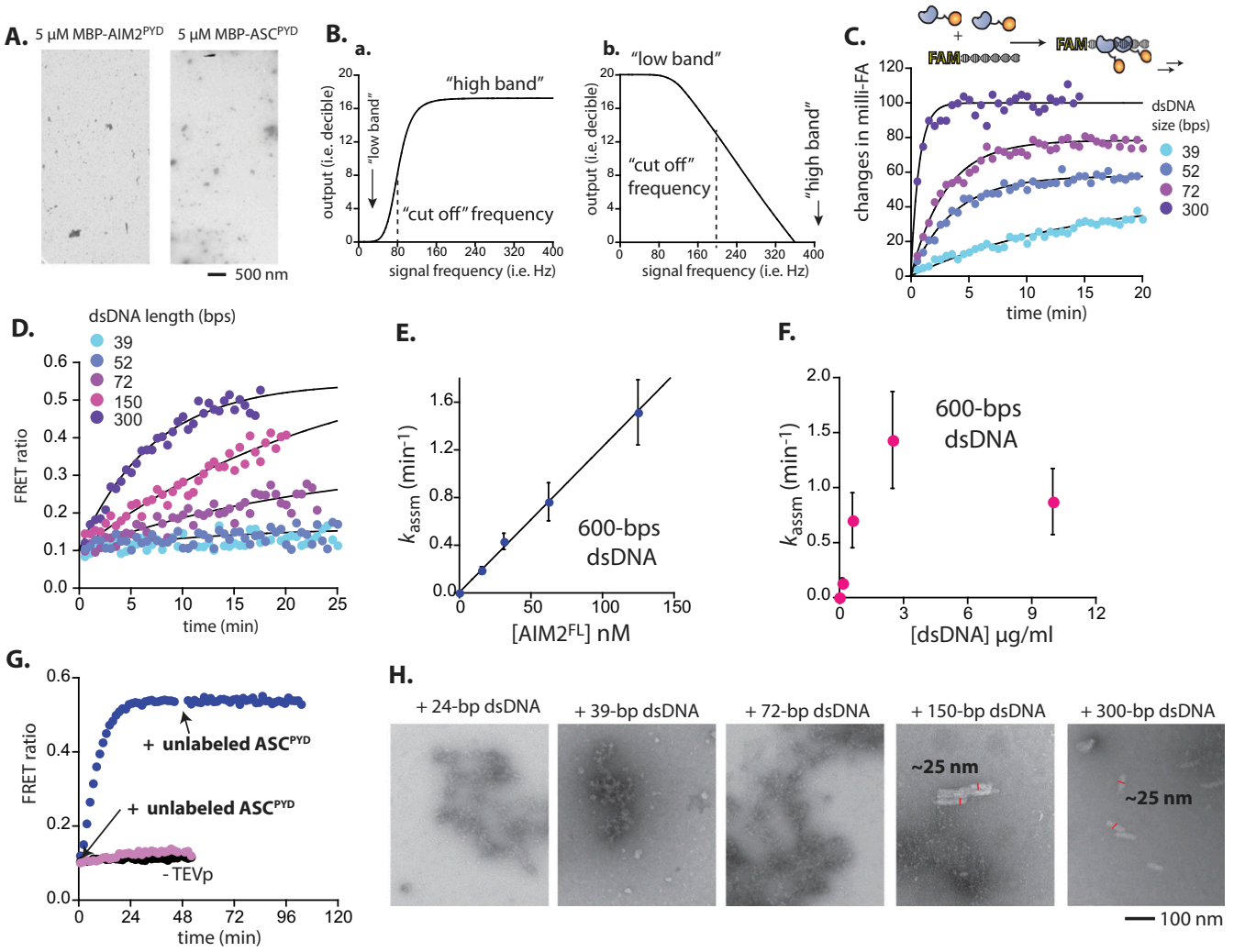

Fig. S1. Additional biochemical data-1. (*A*) Negative-stain electron micrographs of MBP-AIM2^{PYD} and MBP-ASC^{PYD}. Both proteins fail to polymerize when fused to an N-terminal MBP tag. (*B*) Sample response curves of typical a high band-pass filter (*a*) and a low band-pass filter (*b*). Only high-frequency signals are allowed to pass through in the high-pass filter, while the opposite is true in the low-pass filter. (*C*) The time-dependent dsDNA-binding/assembly of AIM2^{FL} (36 nM) on each duplex size (36 nM, binding-site corrected) was monitored using the changes in FA of FAM-labeled dsDNA. Lines are fits to a single-exponential equation. (*D*) The assembly of AIM2^{FL} (36 nM) on each dsDNA size (36 nM, binding-site normalized) was monitored using FRET between labeled proteins. Lines are fits to a single-exponential equation. (*E*) A plot of assembly rates vs. varying concentrations of FRET-labeled AIM2^{FL} in the presence of saturating 600-bp dsDNA (10 μg/mL). The line is a linear fit ($n = 3$; ± SD). (*F*) A plot of assembly rates vs. varying dsDNA concentrations (600 bp) ($n = 3$; ± SD). (*G*) The persistence of the ASC^{PYD} filament was tested as described in Fig. 2*E*. (*H*) Negative-stain electron micrographs of AIM2 (300 nM) in complex with various dsDNA lengths (10 μg/mL).

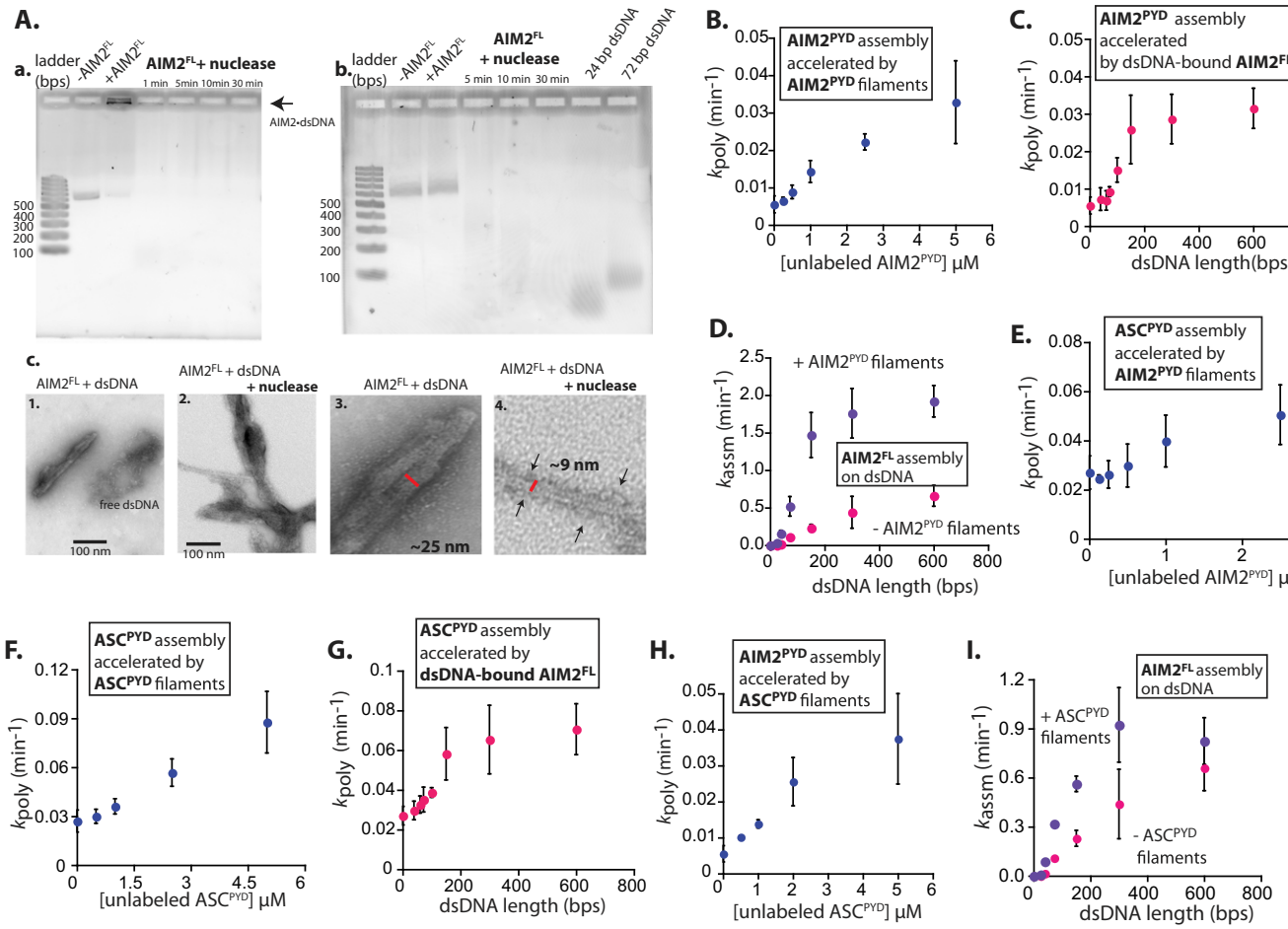

Fig. S2. Additional biochemical data-2. (*A*) Agarose (2.5%) gel electrophoretic mobility shift assays showing dsDNA degradation by micrococcal nuclease (SYBR-gold staining). $CaCl_2$ (5 mM) was supplemented to the reaction buffer, and 50 mM EGTA was added at the given time points to stop the nuclease reaction. (*a*) Without proteinase-K treatment AIM2·dsDNA complexes are essentially immobile in electrophoretic mobility shift assay (1) and (*b*) with proteinase-K treatment to release AIM2-bound dsDNA. In both cases, bound dsDNA is essentially obliterated in 30 min. Synthetic 24-bp and 72-bp dsDNA are shown in *b* as reference. (*c*) Additional negative-stain electron micrographs of 300 nM $AIM2^{FL}$, (*c*, *1*) with 10 µg/mL 600-bp dsDNA and (*c*, *2*) after adding 1 mg/mL micrococcal nuclease and incubating it for 1 h. *c*, *3* is a zoom-in of filaments observed in the presence of dsDNA (*c*, *1*), and *c*, *4* is a zoom-in of filaments observed after DNase treatment (*c*, *2*). Arrows indicate "sprouts" (HIN200 domains). (*B*) A plot of k_{poly}s of FRET-labeled $AIM2^{PYD}$ vs. unlabeled $AIM2^{PYD}$ concentrations ($n = 3$; ± SD). (*C*) A plot of k_{poly}s of FRET-labeled $AIM2^{PYD}$ vs. the length of dsDNA that supports the oligomerization of unlabeled $AIM2^{FL}$ ($n = 3$; ±SD). (*D*) A plot of dsDNA length-dependent k_{assm}s of FRET-labeled $AIM2^{FL}$ in the presence or absence of $AIM2^{PYD}$ filaments ($n = 3$; ± SD). (*E*) A plot of k_{poly}s of FRET-labeled ASC^{PYD} vs. unlabeled $AIM2^{PYD}$ concentrations ($n = 3$; ± SD). (*F*) A plot of k_{poly}s of FRET-labeled ASC^{PYD} vs. unlabeled ASC^{PYD} concentrations ($n = 3$; ± SD). (*G*) A plot of k_{poly}s of FRET-labeled ASC^{PYD} vs. the length of $AIM2^{FL}$-bound dsDNA ($n = 3$; ± SD). (*H*) A plot of k_{poly}s of FRET-labeled $AIM2^{PYD}$ vs. ASC^{PYD} concentrations ($n = 3$; ± SD). (*I*) A plot of dsDNA length-dependent k_{assm}s of FRET-labeled $AIM2^{FL}$ in the presence or absence of ASC^{PYD} filaments ($n = 3$; ± SD).

1. Morrone SR, et al. (2015) Assembly-driven activation of the AIM2 foreign-dsDNA sensor provides a polymerization template for downstream ASC. *Nat Commun* 6:7827.

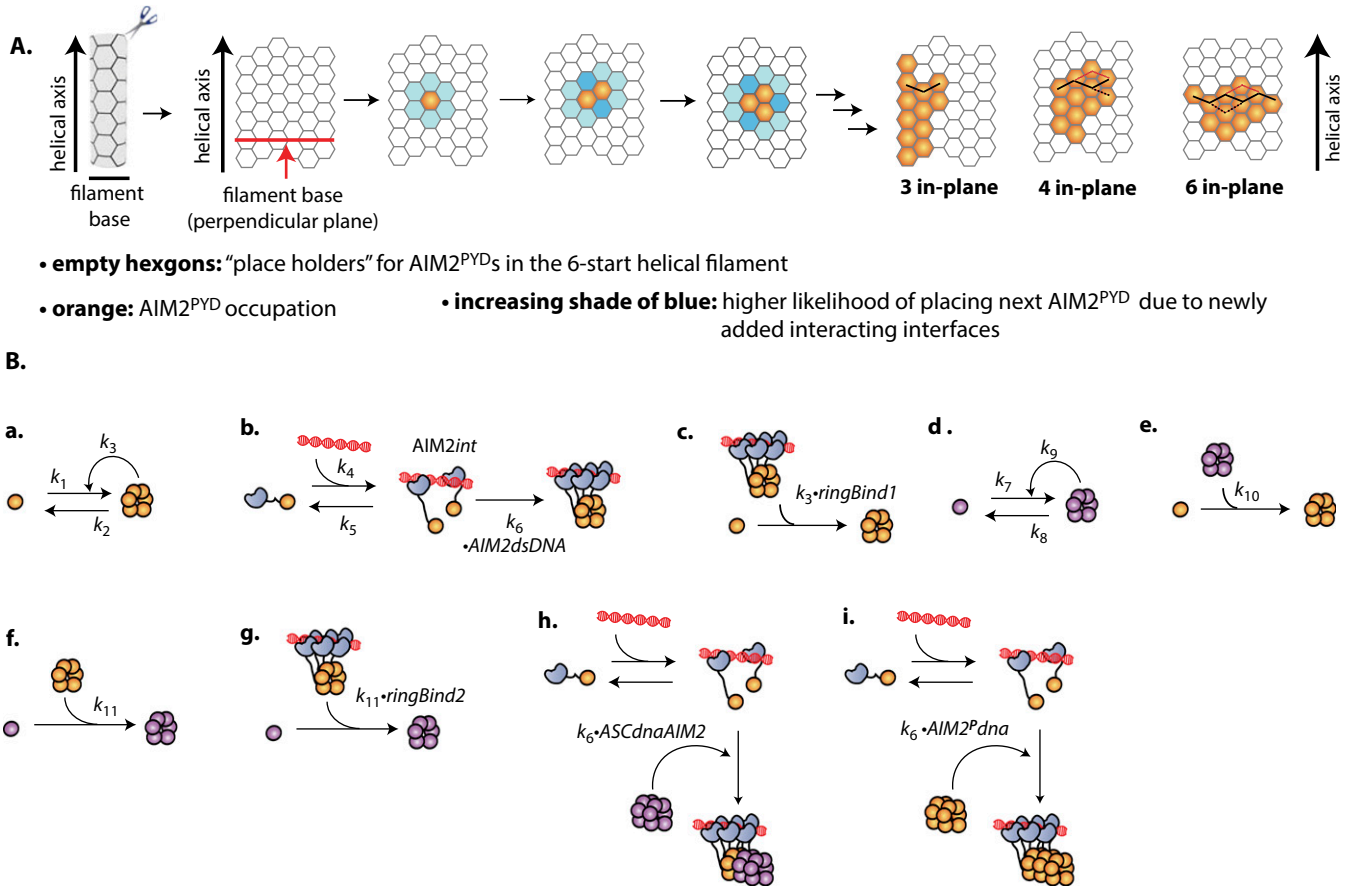

Fig. S3. Modeling of the AIM2-ASC inflammasome assembly. (*A*) A scheme describing our Monte Carlo simulation. The "honeycomb" represents a "butterflied" view of the "empty framework" of the six-start helical filament (the horizontal ends are connected in the simulation). We assumed that the energetic contribution of each of six interfaces is the same, and each AIM2^{PYD} was sequentially added because our experiments indicate that the assembly on dsDNA occurs in a stepwise manner (Fig. 2). (*A*, *Bottom*) Three sample end results of arranging 12 AIM2^{PYD} molecules in the base of six-start filament. The solid and dotted lines indicate different, but equally plausible ways to position AIM2^{PYD}s in-plane. (*B*) Quantitative modeling of the AIM2-ASC inflammasome. (*a*) AIM2^{PYD} polymerizes. AIM2^{PYD} monomers collide with other monomers to form polymers (six-membered ring is shown for simplicity), and resulting polymers accelerate the polymerization of monomers. This process can also be interpreted as *n* of AIM2 monomers are required to nucleate the filament assembly (k_1*[AIM2^{PYD}mono]^*n*) and the filament then subsequently elongates (k_3*[AIM2^{PYD}poly]*[AIM2^{PYD}mono]). We did not include a distinct nucleation species for simplification and treated any AIM2 larger than or equal to a dimer (e.g., $n = 2$) as a polymer. Of note, the FRET signals begin to arise with formation of a dimer, AIM2 requires dsDNA long enough to accommodate at least two molecules for binding/oligomerization (1), and we found $n = 2$ to be sufficient to globally fit our data (likely the lower limit). To implement threshold behavior in protein concentration dependence (i.e., critical concentration), the k_2 value was determined such that (k_3*[*AIM2^{PYD}poly*]*[*AIM2^{PYD}mono*]) = (k_2*[*AIM2^{PYD}poly*]) at $t = \infty$. This simplifies to $k_2 = k_3$*[*critical*], where [*critical*] is the threshold concentration (250 nM). The equation for this process is then

$$d[AIM2^{PYD}poly]/dt = (k_1 * ([AIM2^{PYD}mono] - [critical])\text{^}n) * H([AIM2^{PYD}mono] - [critical]) + (k_3 * [AIM2^{PYD}poly] * [AIM2^{PYD}mono]) - (k_2 * [AIM2^{PYD}poly]) \quad simEqn - 1$$

Note 1: k_1, k_2, and k_3 were used to describe dsDNA-free polymerization of AIM2^{FL} in our simulation. Note 2: *H* is the Heaviside function. (Negative input results in 0; positive input results in 1.) (*b*) AIM2^{FL} binds dsDNA and assembles into nucleoprotein filaments. AIM2 ^{FL} monomers bind dsDNA and form transient, nonfilamentous intermediates (*Aim2^{FL}int*). The existence of intermediates is suggested by our experiments described in Fig. 2. k_4 was set to be fast (non-rate-limiting) to allow the k_6·*AIM2dsDNA* term to be a dominant factor to control the nonlinear dsDNA length and concentration dependences (Fig. 2). k_5 was arbitrarily chosen as a negligible value due to the lack of perceived disassembly. The *AIM2dsDNA* coefficient is a unique numerical value assigned to each dsDNA size. The rate equation for this process is

$$\begin{aligned} d[AIM2\ int]/dt &= (k_4 * [dsDNA] * [AIM2^{FL}]) - (k_5 * [AIM2^{FL}int])) \\ &- (k_6 * AIM2dsDNA * [AIM2^{FL}int] * [AIM2^{FL}int]) \\ &- (k_6 * AIM2dsDNA * [AIM2^{FL}int] * [dsDNA\text{-}bound\ AIM2\ poly]) \\ d[dsDNA\text{-}bound\ AIM2\ polymers]/dt &= (k_6 * AIM2dsDNA * [AIM2^{FL}int] * [AIM2^{FL}int]) \\ &- (k_6 * AIM2dsDNA * [AIM2^{FL}int] * [dsDNA\text{-}bound\ AIM2\ poly]) \end{aligned} \quad simEqn - 2$$

(*c*) dsDNA-bound AIM2^{FL} accelerates the polymerization of AIM2^{PYD}. The *ringBind1* coefficient modifies k_3 to account for dsDNA size dependence, which is a numerical value unique to each dsDNA size. The expanded rate equation for AIM2^{PYD} assembly including this process is then

$$\begin{aligned} d[AIM2^{PYD}poly]/dt &= (k_1 * ([AIM2^{PYD}mono] - [critical])\text{^}n) * \\ &H([AIM2^{PYD}mono] - [critical]) + (k_3 * [AIM2^{PYD}poly] * [AIM2^{PYD}mono]) - (k_2 * [AIM2^{PYD}poly]) \\ &+ (k_3 * ringBind1 * [AIM2^{FL}DNAbound] * [AIM2^{PYD}mono]) \end{aligned} \quad simEqn - 3$$

(*d*) ASC^{PYD} polymerizes. ASC^{PYD} monomers assemble into polymers, and the resulting polymers accelerate the polymerization of monomers. As with AIM2^{PYD} polymerization (***simEqn-1***), This process can also be interpreted as *n* number of ASC monomers are required to nucleate the filament assembly

Legend continued on following page

(k_7*[ASC^{PYD}mono]^n) and the filament then subsequently elongates (k_9*[AIM2^{PYD}poly]*[ASC^{PYD}mono]). As with AIM2^{PYD}, we found that $n = 2$ during global fitting. The monomer concentrations are then reduced by the critical concentration (*critical2* = 0.5 μM). The rate equation for this process is

$$d[ASC^{PYD}poly]/dt = (k_7 * ([ASC^{PYD}mono] - [critical2])\hat{}\, n) * (H([ASC^{PYD}mono] - [critical2]) + (k_9 * [ASC^{PYD}poly] * [ASC^{PYD}mono]) - (k_8 * [ASC^{PYD}poly]) \quad simEqn - 4$$

(*e*) ASC^{PYD} filaments accelerate the polymerization of AIM2^{PYD}. The expanded rate equation for the assembly of AIM2^{PYD} including this process is

$$d[AIM2^{PYD}poly]/dt = (k_1 * ([AIM2^{PYD}mono] - [critical])\hat{}\, n * H([AIM2^{PYD}mono] - [critical]) + (k_3 * [AIM2^{PYD}poly] * [AIM2^{PYD}mono]) - (k_2 * [AIM2^{PYD}poly]) + (k_3 * ringBind1 * [AIM2^{FL}DNAbound] * [AIM2^{PYD}mono]) + (k10 * [ASC^{PYD}poly] * [AIM2^{PYD}mono]) \quad simEqn - 5$$

(*f*) AIM2^{PYD} filaments accelerate the polymerization of ASC^{PYD}. The expanded rate equation for the assembly of ASC^{PYD} including this process is

$$d[ASC^{PYD}poly]/dt = (k_7 * [ASC^{PYD}mono - critical2]\hat{}\, n) * H([ASC^{PYD}mono] - [critical2]) + (k_9 * [ASC^{PYD}poly] * [ASC^{PYD}mono]) - (k_8 * [ASC^{PYD}poly]) + (k11 * [AIM2^{PYD}poly] * [ASC^{PYD}mono]) \quad simEqn - 6$$

(*g*) dsDNA-bound AIM2^{FL} accelerates the polymerization of ASC^{PYD}. The *ringBind2* coefficient modifies k_{11} to account for dsDNA size dependence, which is a unique numerical value for each dsDNA size. The expanded rate equation for ASC^{PYD} assembly including this process is then

$$d[ASC^{PYD}poly]/dt = (k_7 * ([ASC^{PYD}mono] - [critical2])\hat{}\, n) * H([ASC^{PYD}mono] - [critical2]) + (k_9 * [ASC^{PYD}poly]] * [ASC^{PYD}mono]) - (k_8 * [ASC^{PYD}poly]) + (k_{11} * ringBind2 * [AIM2\ DNA\ bound] * [ASC^{PYD}mono]) \quad simEqn - 7$$

(*h*) ASC^{PYD} polymers accelerate the assembly of AIM2^{FL} on dsDNA. The *ASCdnaAIM2* coefficient, a numerical value unique to each dsDNA size, modifies k_6 to account for the observed dsDNA length dependence (Fig. 6 *C* and *D*). The expanded rate equation for AIM2^{FL} assembly on dsDNA including this process is then

$$d[dsDNA\text{-}bound\ AIM2\ polymers]/dt = (k_6 * AIM2dsDNA * [AIM2^{FL}int] * [AIM2^{FL}int]) + (k_6 * AIM2dsDNA * [AIM2^{FL}int] * [dsDNA\text{-}bound\ AIM2\ poly]) + (k_6 * ASCdnaAIM2 * [ASC^{PYD}poly] * [AIM2^{FL}int]) \quad simEqn - 8$$

(*i*) AIM2^{PYD} polymers accelerate the assembly of AIM2^{FL} on dsDNA. The *AIM2^{p}dna* coefficient, a numerical value unique to each dsDNA size, modifies k_6 to account for the observed dsDNA length dependence (Fig. 4 *E* and *F*). The expanded rate equation for AIM2^{FL} assembly on dsDNA including this process is then

$$d[dsDNA\text{-}bound\ AIM2\ polymers]/dt = (k_6 * AIM2dsDNA * [AIM2^{FL}int] * [AIM2^{FL}int]) + (k_6 * AIM2dsDNA * [AIM2^{FL}int] * [dsDNA\text{-}bound\ AIM2\ poly]) + (k_6 * ASCdnaAIM2 * [ASC^{PYD}poly] * [AIM2^{FL}int]) + (k_6 * AIM2^{p}dna * [AIM2^{PYD}poly] * [AIM2^{FL}int]) \quad simEqn - 9$$

1. Morrone SR, et al. (2015) Assembly-driven activation of the AIM2 foreign-dsDNA sensor provides a polymerization template for downstream ASC. *Nat Commun* 6:7827.

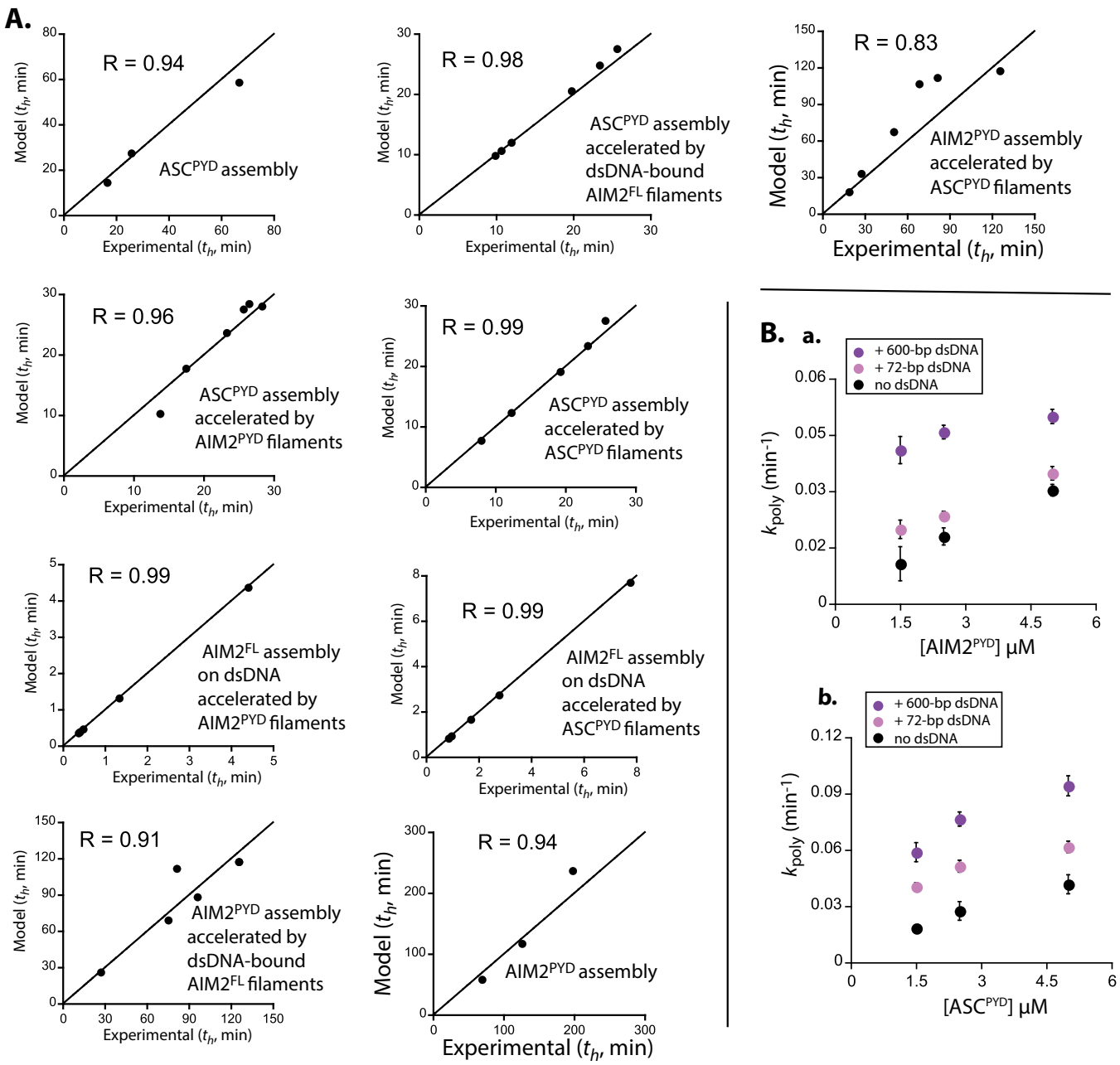

Fig. S4. (*A*) Additional plots of model vs. apparent t_h. (*B*) AIM2^{FL}·dsDNA complexes can accelerate the polymerization of different concentrations of FRET-labeled AIM2^{PYD} (*a*) and ASC^{PYD} (*b*) in a dsDNA length-dependent manner (n = 3; ± SD).

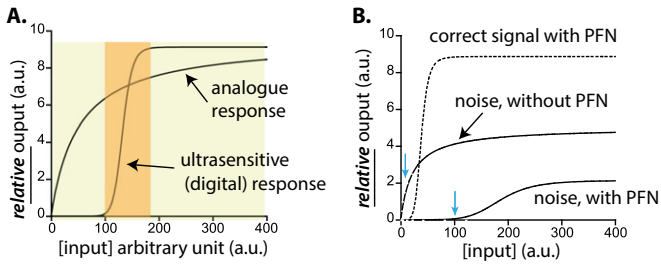

Fig. S5. (*A*) An exemplary plot demonstrating an ultrasensitive (digital) system vs. analog system. The shaded areas indicate the range of input concentrations that induces the most dynamic changes in output (orange: ultrasensitive; yellow: analog). In the analog system the output changes immediately with increasing input, but the change also occurs gradually over a broad range. In the ultrasensitive system not only is a higher input concentration required to trigger changes in output, but such a change also occurs over a much narrower input range in a switch-like manner (digital). (*B*) An exemplary plot demonstrating how PFN would attenuate noise. Without PFN (analog), the system responds immediately with increasing noise, albeit much less efficiently compared with the correct signal (e.g., compared the analog response in Fig. S5*A*). With PFN, the system does not respond until the noise reaches a much higher concentration (blue arrows). Moreover, the overall change in relative output is smaller when PFN is present. The dotted line shows how the correct signal would influence the output in the presence of PFN.

Other Supporting Information Files

Dataset S1 (PDF)
Dataset S2 (TXT)
Dataset S3 (XLSX)